Available online at www.sciencedirect.com

SCIENCE DIRECT®

Journal of Applied Geophysics 57 (2005) 306–326

JOURNAL OF APPLIED GEOPHYSICS

www.elsevier.com/locate/jappgeo

Nondestructive imaging of small size voids at Akrotiri archaeological site, Thera Island, Greece, by seismic inversion techniques

Filippos I. Louis[a,b,*,1], Roger A. Clark[a], Ioannis F. Louis[b], Costas C. Makropoulos[b]

[a]*School of Earth Sciences, University of Leeds, Leeds LS29JT, UK*
[b]*Department of Geophysics and Geothermic, University of Athens, Panepistimiopolis, Ilissia, Athens 15784, Greece*

Received 21 January 2004; accepted 11 April 2005

Abstract

High-resolution travel time tomography was used to explore the volcanic basement rock at the Akrotiri archaeological site, Thera (Santorini) Island. The survey was carried out in the context of a large scale project, in which the protective roof cover of old monuments is being replaced by a new environmentally friendly structure, which will be supported by 95 pillars drilled into the volcanic basement rock. Man-made or natural cavities (empty or half-filled with stones), ceramics, and other materials of archaeological interest were unveiled during the excavation of foundation shafts. The objective of this geophysical investigation was the detection of such voids in the vicinity of the excavated shafts, so that the overhead structure can be better supported and protected in the case of an earthquake event. The cross-hole seismic tomography technique was adopted for this purpose. A number of synthetic examples and a calibration experiment at a shaft with a known natural cavity clearly indicated that the tomographic inversion is capable of providing high-resolution 2-D velocity models. High S/N ratios ensured field seismic records of high quality. A set of stability tests was run to check the consistency of the method. Travel time residuals verified the validity of the final velocity depth sections, while model complexity trends showed a consistency between models after a certain number of iterations. The reconstructed velocity fields were quite consistent with the expected velocity structures based on the geologic descriptions of formations encountered during the drilling of the shafts. Impressive low-velocity structures attributed to natural or man-made cavities were reported to the constructing group of engineers, and a remedial action plan was being undertaken to support and improve the ground behavior.

Keywords: Travel time tomography; Inversion; Geophysical applications in archaeometry; Akrotiri archaeological site, Thera Island; Cross-hole; VSP

* Corresponding author. Department of Geophysics and Geothermic, University of Athens, Panepistimiopolis, Ilissia, Athens 15784, Greece.
E-mail addresses: flouis@geol.uoa.gr (F.I. Louis), R.Clark@earth.leeds.ac.uk (R.A. Clark), jlouis@geol.uoa.gr (I.F. Louis), kmacrop@geol.uoa.gr (C.C. Makropoulos).
[1] Formerly University of Leeds, School of Earth Sciences, Leeds, LS29JT, UK.

0926-9851/$ - see front matter © 2005 Elsevier B.V. All rights reserved.
doi:10.1016/j.jappgeo.2005.04.001

1. Introduction

In the past decade, seismic tomography has been routinely used as a geophysical tool for investigating velocity variations in different geological environments. Benefiting from ongoing developments of down-hole seismic sources and seismometers, cross-hole seismic tomography, in particular, is now perhaps the best solution for creating high-resolution maps of seismic properties representative of the geologic cross sections between boreholes. The use of cross-hole seismic tomography as a subsurface structural information extraction tool has been extensively discussed in the geophysical literature. In its early days more than 30 years ago (Bois et al., 1971), the technique was seen as a logical extension of concepts used in medical tomography having the potential of yielding high-resolution structural information. However, 30 years of testing (e.g., Dines and Lytle, 1979; Mason, 1981; Peterson et al., 1985; Bregman et al., 1989; Pratt and Chapman, 1992; Pratt et al., 1993; Rector et al., 1996; Washbourne et al., 1998) have proven that there is much about the method that is different and more difficult than medical tomography. Such complicating differences include insufficient ray coverage, dispersive and anisotropic wave propagation, and multiple arrival paths. In a layered environment, cross-hole data are certain to contain arrivals from multiple paths, guided wave modes, super critical reflections, and mode conversions. From all such arrivals, the least ambiguous source of information in cross-hole surveys is direct arrivals. In recent papers (e.g., Pratt and Goulty, 1991; Khalil et al., 1993; Lazaratos et al., 1993; Schaack, 1995; Bube and Langan, 1995), reflected and other arrivals have been used in conjunction with the direct arrivals to increase the resolution and stability of the solution. In this paper, cross-hole seismic tomography and vertical seismic profiling (VSP) methods are used to investigate small size structures, such as voids, unveiled during foundation activities at an archaeological site in Greece.

2. History and problem description

The Akrotiri archaeological site (Fig. 1) is one of the most important prehistoric settlements of the Aegean Sea. The first habitation of the site dates from the late Neolithic period. During the early Bronze Age, a sizable settlement was established, which was extended and gradually developed into one of the main urban centers and ports of the Aegean Sea during the middle and early Late Bronze Age. The large extent of the settlement, the elaborate drainage system, and the sophisticated multi-storey buildings with their magnificent wall paintings, furniture, and vessels showed its great development and prosperity. The town's life came to an abrupt end in the late 17th century BC when the inhabitants were forced to abandon the city as a result of severe earthquakes. A massive volcanic eruption followed, which resulted in volcanic material covering the entire island and the town itself. Ironically, this material ended up protecting and preserving the buildings and their contents, just like in Pompeii.

Currently, the protective roof cover of the old monuments at Akrotiri is being replaced by a new elaborate and environmentally friendly structure. The new structure will be supported by 95 pillars embedded within an equal number of excavated shafts filled with concrete. The foundation shafts (1.2 m in diameter and approximately 8 m in depth) penetrate through the existing prehistoric settlement as found today, an underlying layer of old ruin material of variable thickness, and ultimately terminate in the pyroclastic volcanic basement rock (Fig. 2). The top of the pyroclastic formation is found at depths varying between 2 and 15 m below the ground surface. During the shaft excavation, man-made cavities were discovered within the pyroclastic formation. Some of these cavities were empty while others contained stones, ceramics, and other materials. Although the unveiled cavities are of great importance to archaeologists, they nevertheless pose a technical challenge to civil engineers because they raise questions about the stability of the new roof cover.

The Department of Geophysics of the University of Athens was commissioned by the Archaeological Society of Athens to carry out an extended geophysical survey at Akrotiri to investigate the problem of cavities. From the beginning, it became obvious that conventional surface geophysical methods could not be used to address the problem for two reasons: (a) the masking effect caused by the highly attenuative loose layer of older ruins made the detection of voids or other geometrical subsurface features laying underneath rather unlikely; and (b) due to the archaeological nature of the site surface, activities are strictly prohib-

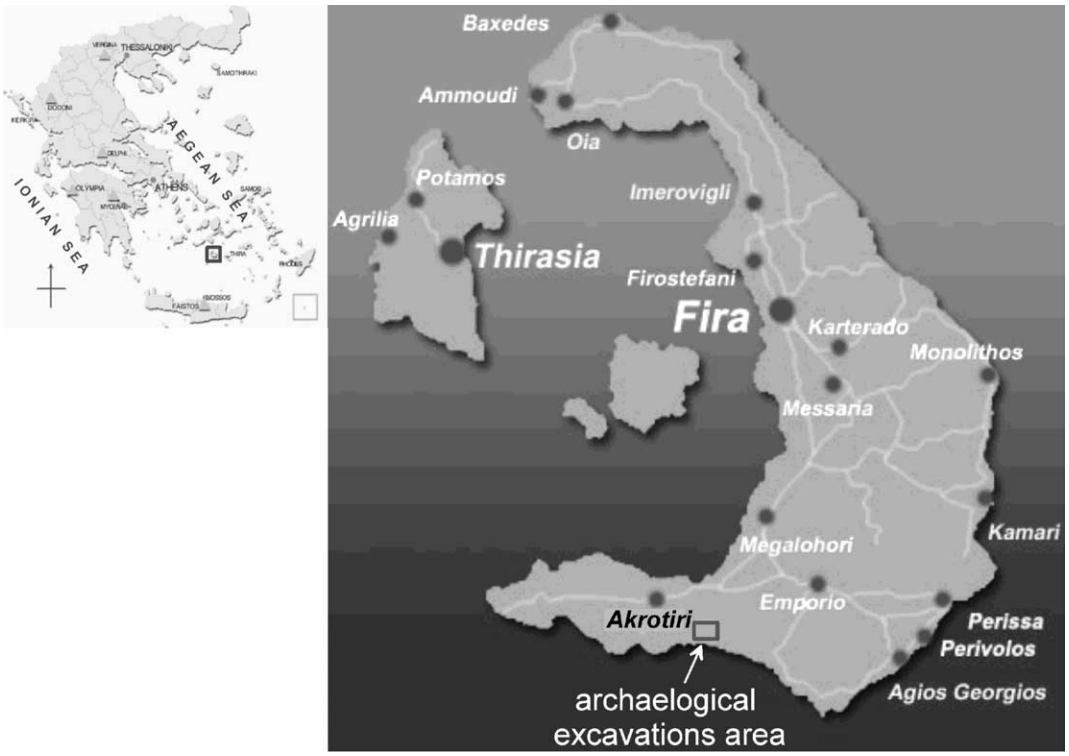

Fig. 1. Thera Island with the location of the investigated area (map of Greece taken from http://www.culture.gr, Map of Thera taken from http://www.greecetravel.com/aegean/map_of_santorini_island.htm).

ited. Fortunately, the existence of the excavated shafts offered an excellent opportunity to apply cross-hole seismic techniques for solving the problem. Using such techniques offers two distinct advantages. First, the seismic attenuation issue associated with propagation through the near-surface layer is bypassed. Second, the high-frequency bandwidth of the seismic source is preserved during propagation in the inter-shaft area of interest, thus providing an opportunity for obtaining high-resolution images. The seismic cross-hole and VSP experiments presented in this paper were designed and

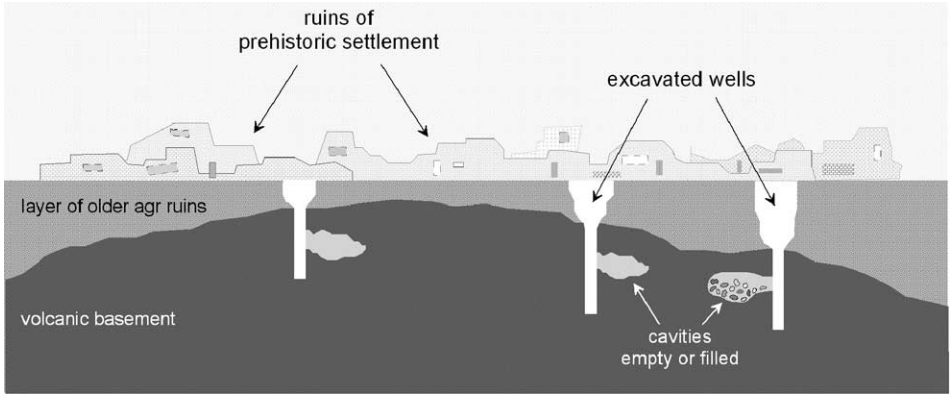

Fig. 2. Cross-section sketch of Akrotiri archaeological site.

carried out in order to detect possible bedrock cavities and in turn improve the stability of the new roof structure in the case of an earthquake.

3. Seismic tomography using the algebraic reconstruction technique (ART)

As with any geophysical problem, a forward modeling algorithm, an inversion algorithm, and a parameterized description of the medium need to be considered for use with cross-hole seismic travel time data. In this particular case, the region, bordered by the two boreholes, is divided into rectangular cells or pixels. The velocity of each cell is assumed to be constant and unknown.

In smooth models with low-velocity contrasts, the assumption of straight rays dramatically reduces the computational effort, when compared to a full ray-bending inversion, because the problem becomes linear. However, for large velocity contrasts, the straight ray approximation gives unacceptable results because it introduces a considerable amount of smoothing to the resulting velocity tomogram. This ray dependence on the slowness field makes the problem highly nonlinear. The problem can be linearized by considering a small perturbation of the slowness about a reference slowness field. As a rule of thumb, velocity contrasts of up to 15% are handled within tolerance by straight ray inversion (Hatton et al., 1986).

A considerable number of modeling and inversion schemes can be found in the literature (McMechan, 1983; Smith, 1984; Peterson et al., 1985). In comparison to matrix inversion methods and other iterative techniques (simultaneous iterative reconstruction technique, SIRT; conjugate gradient, CG), the algebraic reconstruction technique (ART) possess several advantages and was the inversion scheme adopted in this project. The specific inversion technique was chosen since it is one of the two iterative methods (the other one being SIRT) used by the tomographic software, CAT3D (Vesnaver et al., 1999). ART is, in general, faster, particularly when handling large data sets, compared to direct matrix inversion since the latter solves all equations simultaneously and requires a large amount of computer memory to store the ray equation sparse matrix elements. Moreover, ART treats each equation separately in a more efficient way; constraints can be easily incorporated to accommodate any prior knowledge of the medium and is computationally faster than any other iterative scheme (Smith, 1984).

The algebraic reconstruction technique (ART) is trying to approach the observed data while iteratively adjusting in small steps the values of the parameters. Starting by guessing a solution to all of the parameters, the travel time of the first ray is calculated. For each ray, the difference between the calculated time and the observed time is regarded as the error, and it is distributed equally along the ray path. The update equation that provides the improved solution is:

$$\Delta p_{ij} = \frac{\Delta t_i l_{ij}}{\sum_j l_{ij}^2}. \quad (1)$$

If we consider t_i to be the first-arrival travel time for the ith ray connecting a seismic source and receiver, and let l_{ij} be the distance traveled across the jth cell by the ith ray, and p_j be the slowness of the jth cell, then Δt_i is the change in t_i due to the cumulative effect of all changes Δp_{ij} in the parameters along the ray p_{ij}.

The updating scheme of Eq. (1) makes some intuitive sense. If the denominator is considered as a measure of the square of the total ray length L_i, then $\Delta t_i/L_i$ is the total slowness error. The remaining factor l_{ij}/L_i is the proportion of the ray in a particular pixel. The product of these two factors gives the slowness error proportionally assigned to the pixel.

ART attempts to honor the observed data while iteratively altering in small steps the values of the parameters. This process continues until all equations have been solved once. The procedure returns to the first equation and the set of equations is sequentially solved again. The whole process is repeated until the parameters are not varying significantly, or the time residuals drop under an assigned threshold.

4. Geological setting and field experiments

The survey was carried out at the archaeological excavation area of Akrotiri located on the southern tip of Santorini Island (Louis and Makropoulos, 2001). Santorini is an active volcano in the South Aegean Sea about 120 km north of Crete and belongs to the Cycladic islands (Fig. 1). The oldest volcanic rocks are found on the Akrotiri peninsula and the Christiana

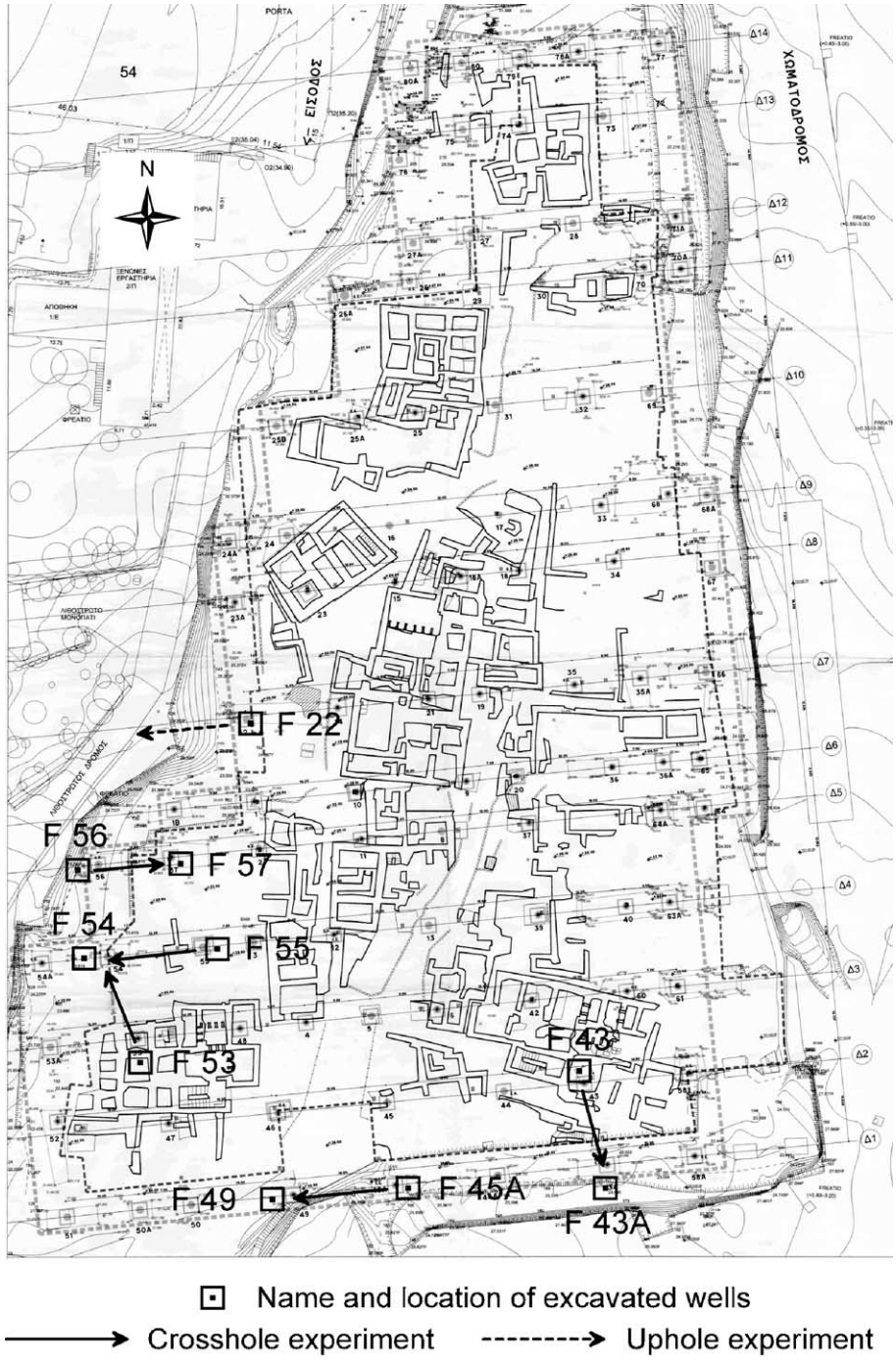

Fig. 3. Ground plan map of the archaeological area with the locations of the excavated wells (J&P Hellas et al., Constructing Group of Engineers, 2001).

islands. These rocks are composed of dacitic lavas that updomed the sea floor and produced various flows and pyroclastic deposits but have been strongly altered by hydrothermal activity. The updomed areas are still well visible at the Akrotiri peninsula. From marine fossils embedded in the tuffs, a minimum age of 2 million years has been determined for the Akrotiri peninsula. At the localities of Balos ("Red Beach"), Kokkinopetra, Mavropetra, and Mavrocachidi, basaltic to andesitic strombolian scoria cones that flank the Akrotiri volcanoes are exposed. The shafts in the excavation area were drilled into the volcanic basement rocks (pyroclastic formation) that consist of volcanic breccias up to volcanic tuffs, comprising of cemented stones and/or lava balls (diameter up to 50 cm). Fig. 3 shows the ground plan map of the investigated area with 70 total locations where cross-hole VSP seismic experiments took place. Six among the 70 cases were selected to be involved in this study since they are the most important from the archaeological point of view.

The field data sets analyzed include cross-hole experiments between shafts F43A–F43, F56–F57, F54–F55, and F49–F45A, and a VSP experiment in shaft F22. Two of them (F43A–F43 and F22) were carefully chosen as representatives for further statistical and error analyses (Louis, 2001). The first and second shafts in each pair served as the transmitting and receiving shafts, respectively. Shaft F22 served as the transmitting shaft for the VSP experiment. A steel casing ring of 1 m height was used to support the head of the shaft from falling rocks from the loose weathered pyroclastic material. A string of twelve 14 Hz vertical geophones was lowered in each receiving shaft (Fig. 4) with the geophones placed oblique to vertical at a spacing of 0.5 m. The same spacing was used as the vertical inter-distance between seismic sources for all the cross-hole experiments.

In the VSP experiment conducted in shaft F22, geophones with spacings varying between 0.3 and 0.5 m were spread on the ground surface along a straight line ending at the head of the shaft. Ten grams of dynamite charges triggered with seismic caps was used as seismic source fired at 0.5 m vertical increments from the bottom to the top of the transmitting shafts, leading to a total number of 12 shots. Dynamite, as a high-frequency impulsive source, was proven to be the appropriate source producing clear onsets in the highly attenuating environment of volcanic dust.

Seismic signals were recorded by a Strata View R48 recording system of EG&G with a sampling rate of 0.125 ms. In most of the cross-hole experiments (shafts F56–F57, F54–F55, and F49–F45A), 13 shots were fired except from the case of the F43A–F43 investigation in which 15 shots were fired. Trans-

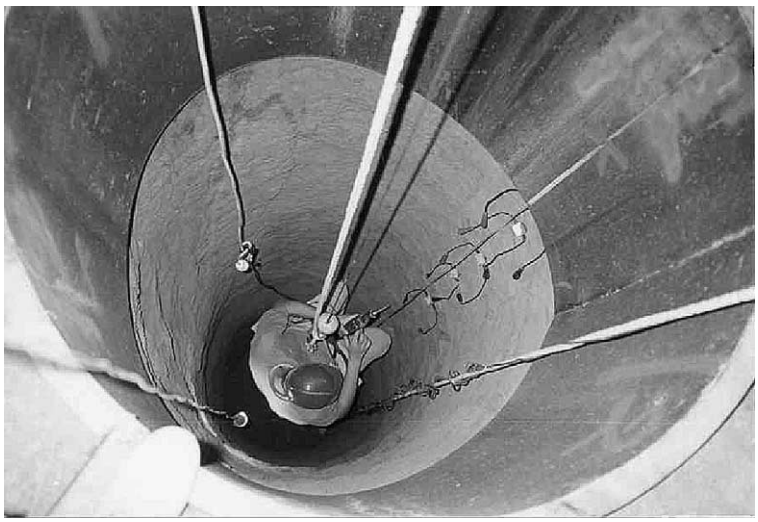

Fig. 4. Receiver string inside the excavated shafts.

mitted signals were recorded from 11 geophones in all cases (the first channel was not working) and their respective P-wave travel times were measured. High S/N ratios ensured field seismic records of high quality and first arrival times were handpicked from the raw data sets with an accuracy better than $0.25 \pm$ ms. Typical common shot gathers examples from cross-hole and VSP data sets are shown in Fig. 5.

5. Demonstration of the solution technique

The inversion method was tested by using a synthetic data set in order to demonstrate that the reconstruction capability of the algorithm is efficient and the convergence to the correct solution can be achieved after a certain number of iterations. The checkerboard test (Leveque et al., 1993) was applied for this purpose. In this procedure, a box-car velocity function is used to generate the velocity variations in the synthetic model. The amplitude of the box-car function depends on the velocity contrast expected in the investigated area. For specific source/receiver geometry, the model response is calculated. First arrival travel times were generated using a two-point ray tracing scheme that is part of the tomographic software CAT3D, and the travel time data were contaminated with uniform random noise (~ 3%), with zero mean and amplitude $\pm b$, where b is a value chosen based on the ratio of maximum–minimum observed travel times. The inverse problem was then solved using the ART method while regarding the computed synthetic times as the observed data. Linear and non-linear schemes were tested, and the percentage of the reconstructed initial model was considered as the recovering capability of this solution technique.

Two checkerboard tests were performed for the two acquisition geometries adopted in the experiments. A total number of 300 square pixels were used for each case, while the variation of the velocity function was assigned from the literature. The cell size used both in the numerical simulations and the real experiments was approximately 0.5 m. Since the objective of the tomographic survey was to detect and locate cavities in the pyroclastic basement rock, a velocity contrast of

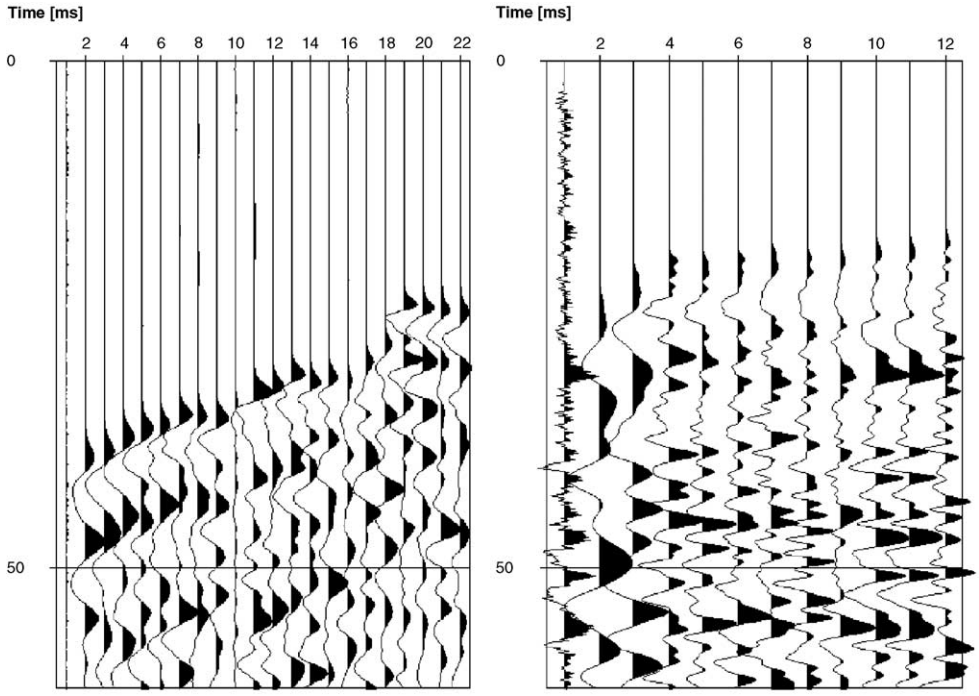

Fig. 5. Typical seismic records from cross-hole F43A–F43 (a) and VSP experiment F22 (b).

350/850 m/s was chosen to represent the velocity in the air and the average velocity of the pyroclastic formation. A seismic velocity of 500 m/s served as the initial homogeneous model to carry out the inversion (Fig. 6a). The checkerboard model was constructed in such a way as to test if velocity anomalies with dimensions of 2–3 m can be reconstructed. After a certain number of iterations, it was evident that the starting velocity model was not of such importance since it could be varied between 400 and 800 m/s with no major effect on the final solution. The relative invariance of the final solution to the initial guess has been encountered previously by the authors when utilizing ART methods with high-quality data sets. Since ART is a row action method and each equation is solved separately, the starting model is mainly perturbed from the early ray paths—equations. This is the reason why the most accurate travel times were incorporated at the beginning of the inversion process.

The resulting velocity tomogram obtained from linear inversion using the straight ray approximation (Fig. 6b) is acceptable since the true model is satisfactorily reconstructed. The main distortion and ambiguity in the solution occur at the edges of the tomogram where the ray coverage is extremely poor or even absent. However, since the ray curvature should not be ignored, a two-point ray tracing algorithm was applied and the non-linear iterative scheme was implemented. In this case, the number of iterations and the

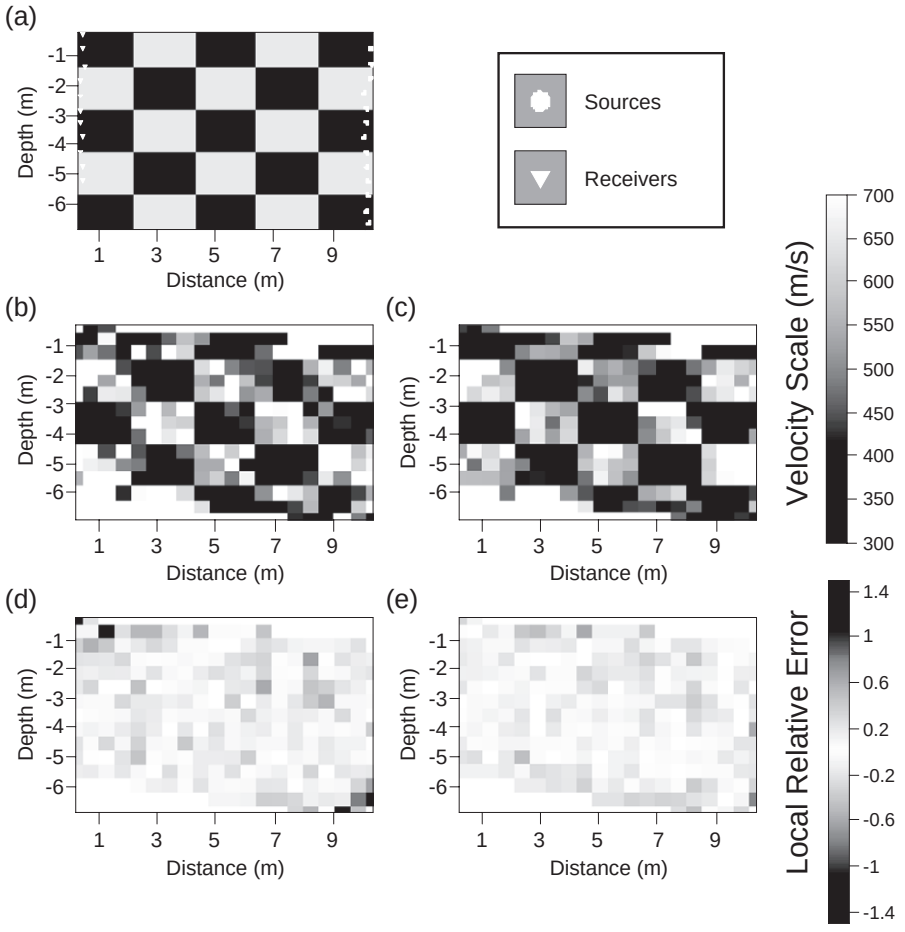

Fig. 6. True model (a), reconstructed velocity tomograms for the cross-hole checkerboard test, using linear (b) and non-linear (c) inversion and their corresponding local relative error maps (d and e).

starting velocity model were kept the same as before without any velocity constraints during the inversion. The solution tomogram is shown in Fig. 6c.

By comparing Fig. 6b and c, it appears that the non-linear procedure gives better results. The geometrical shapes and values of the model parameters are defined more precisely. The reconstruction percentage error e was calculated for both inversion schemes by using the formula:

$$e = \frac{V_{i_{\text{final}}} - V_{i_{\text{initial}}}}{V_{\text{average}}}$$

where $V_{i_{\text{initial}}}$ is the ith pixel's velocity in the starting model, $V_{i_{\text{final}}}$ is the ith pixel's velocity after the final

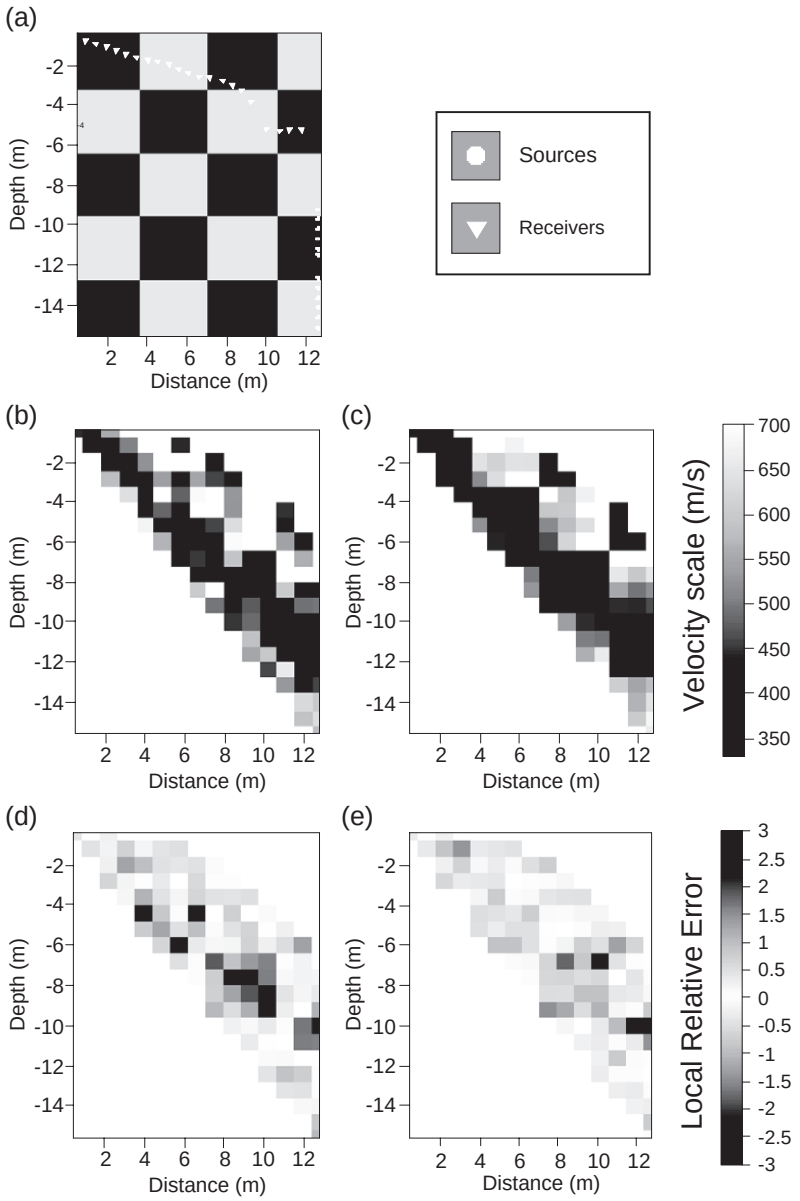

Fig. 7. True model (a), reconstructed velocity tomograms for the VSP checkerboard test, using linear (b) and non-linear (c) inversion and their corresponding local relative error maps (d and e).

iteration, and V_{average} is the average value of the input velocity model (600 m/s). The maximum divergence between recovered and true models in both reconstructions is less than 7%, indicating in this way the accuracy of the inversion scheme. Furthermore, the local relative error LRE was computed and plotted for each pixel (Fig. 6d and e):

$$LRE = \frac{V_{i_{\text{true}}} - V_{i_{\text{final}}}}{V_{\text{true}}}$$

where $V_{i_{\text{true}}}$ is the ith pixel's true velocity. The whole procedure was repeated for the VSP experiment and a new checkerboard test was constructed with the same characteristics as in the cross-hole case.

Even though numerical simulations utilizing checkerboard patterns are, in general, very unforgiving concerning the reconstruction of the original model, in this case, the majority of the inverted models was, to a certain extent, satisfactory recovered, mostly as a result of the appropriate choice of cell size given the restricted aperture, ray coverage, and noise added on data.

Fig. 7a, b, and c, respectively, display the initial velocity model and the inversion results both for linear and non-linear procedures along with their respective local relative error maps (Fig. 7d and e). Comparing the final reconstructed images between the cross-hole and the VSP synthetic examples for the linear and the non-linear cases, it is obvious that better recovery of the model is achieved using cross-hole data (maximum reconstruction errors <5%). The poorer model restoration (maximum errors <7%) obtained in the VSP synthetic examples is due to the limited angular ray coverage in these models. However, even in this case, due to the large amount of ray paths involved, the solution is not unconstrained and a good-enough representation of the initial model is obtained. The consequence of noise in the data is mostly evident in the linear experiments since error-free travel times accomplished slightly better reconstructions.

6. Application of first arrival travel time tomography

High S/N ratios ensured field seismic records of very good quality. Spectral analysis over a time window around the direct arrivals indicated a dominant frequency of 300 Hz with even higher frequencies, up to 500 Hz, present in the cross-hole experiments. Model parameterization was the same as the one adopted in the checkerboard tests, leading to a total number of 300 square pixels for each model. A homogeneous velocity field of 850 m/s, representing an average velocity for pyroclastic formations taken from the bibliography (150–1500 m/s; Koloski et al., 1989), was chosen as an initial guess to start the inversion.

Raw velocity models were firstly obtained by utilizing linear inversion schemes, which in turn were used as initial guess for nonlinear inversion processing to obtain the final velocity models. Although it can be computed very easily, the measure of ray density is considered rather a poor indicator of the local reliability because it does not distinguish linearly dependent from independent rays. Singular value decomposition and null space energy indicators are used today along with ray density to estimate the reliability of the solution (Bohm and Vesnaver, 1999). However, this analysis was not numerically feasible in this project and thus was not applied. Inspection of the model perturbations during the inverse procedure showed in both experiments that stability on the solution occurred after the 15th iteration.

7. Quantifying performance

A crucial step in the inversion procedure is the determination of the amount of error associated with the solution. A major source of ambiguities in the estimates of the velocity field (Bohm and Vesnaver, 1999) is the inadequate acquisition geometry for illuminating the desired target. In addition, the forward ray tracing problem is not solved exactly and the resulting approximations can introduce errors. Moreover, the use of arrival times rather than complete waveforms, and the simulation of real geologic structures by a simplified blocky earth model, while they speed up inversion, nevertheless are approximations of the forward modeling procedure.

The major goal when performing an inversion is to minimize an objective function, which usually consists of a roughness or complexity-weighted term, and

the data residuals part. Philips and Fehler (1991) define the solution roughness as the sum of the squares of horizontal and vertical second differences of the model slowness values taken throughout the solution. In contrast, many authors use a regularizing function $F(m)$, which measures the departure of a sought-after model m from a particular reference model m_{ref}, that is:

$$F(m) = m - m_{\text{ref}}. \quad (2)$$

Since the tomographic solution was tested and found almost independent of the initial model, the above regularizing function (Eq. (2)) was used as a statistical tool to observe the numerical oscillations in the model's slowness values between iterations.

8. Data errors and model complexity

A number of tests were performed on the two representative data sets to provide a quantitative assessment of errors in the inverted data. The first was the travel time residuals or data misfit, indicating how well the observed travel time data are predicted by the solution velocity models. Furthermore, for every one of the experiments, the RMS data residual was calculated:

$$\text{RMS\_data\_residual} = \sqrt{\left(\frac{1}{N}\sum_{i=1}^{N}(t_i^{\text{o}} - t_i^{\text{c}})^2\right)}$$

where t_i^{o} and t_i^{c} stand for observed and calculated (synthetic) travel times, and N represents the number of travel time data (Table 1).

Following this procedure, synthetic travel times computed for the final velocity models were plotted against the observed travel time data. Figs. 8 and 9 show typical examples of plots of the observed and modeled travel times for the first common shot gather for both types of experiments.

Table 1
RMS error of travel time data

Shaft number	Data RMS
F43A–F43	1.25
F22	0.79
F57–F56	0.82
F55–F54	0.59
F45A–F49	0.34

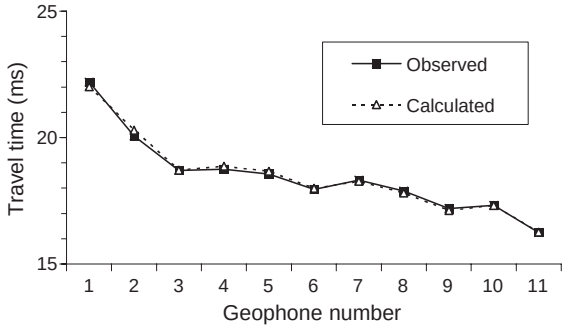

Fig. 8. Comparison plot of observed and computed travel times for the cross-hole experiments F43A and F43.

The low average deviations (<0.3 ms) ensure very good fits between observed and modeled travel time curves. A common convergence criterion in an inversion procedure is when the misfit value reaches the picking error. The tomographic process in all experiments was terminated once the RMS error was not varied significantly. Figs. 10 and 11 show plots of the mean absolute errors calculated for both experiments during the iterative procedure. For the cross-hole case (Fig. 10), it is obvious that the mean misfit drops quickly during the first five iterations, reaching asymptotically the value of 0.1 ms right after the 10th iteration, which is considerably below the effective picking error (0.25 ms).

In the VSP case, the mean absolute value (Fig. 11) rapidly drops after the first iteration, stabilizing around 0.6 ms for the remaining iterations. The

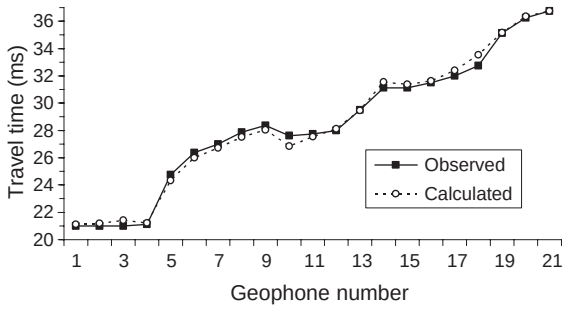

Fig. 9. Comparison plot of observed and computed travel times for the VSP experiment F22.

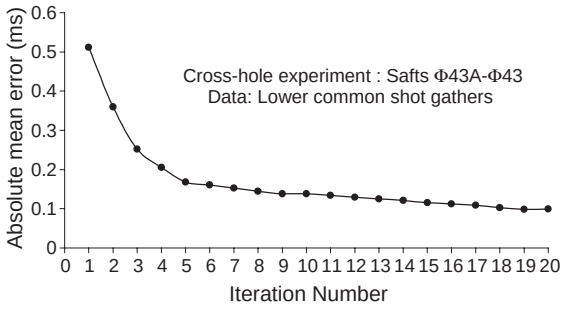

Fig. 10. Typical plot of mean absolute travel time for the cross-hole experiments F43A and F43.

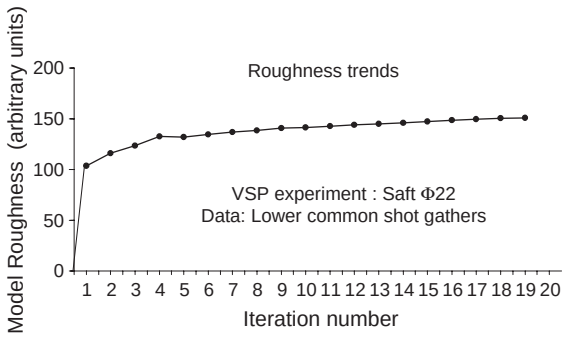

Fig. 12. Typical plot of complexity trends versus iteration number for the VSP experiment F22.

higher residual value in this layout indicates that the unknown parameters are not significantly constrained due to the quite limited angular coverage of rays.

Apart from the travel time residuals, a second test of error assessment was performed concerning the model complexity function, mcf:

$$\mathrm{mcf} = \sqrt{\frac{\sum (V_i - V_{i_0})^2}{N}}$$

where V_i is the velocity value of the ith pixel, V_{i_0} is the average velocity of the initial model, and N is the number of pixels composing the model. Starting with an initial velocity model and after a number of iterations, the complexity function should increase asymptotically to a plateau representing the misfit of a best-fitted model. Following this procedure, the complexity functions for the same selected experiments used previously in conjunction with the data residual RMS error were computed. Figs. 12 and 13 show the complexity graphs for both acquisition layouts, where the oscillation of the model parameters in the cross-shaft case (Fig. 13) stabilizes after seven iterations, indicating in a way that the model subspace is confined. In the VSP experiment (Fig. 12), the oscillations in model perturbations drop significantly after about 11 iterations. In both tomographic procedures, a steady trend is achieved in the last three to four iterations, indicating in some way the uniqueness of the solution.

Finally ray density maps (Figs. 14–16) were constructed to provide an impression of the reliability of the final velocity tomograms. As expected, the ray coverage in the cross-hole layouts is less intense at the top and bottom areas of the models—a fact that explains the poorer reconstructions of these parts in the numerical experiments. The different acquisition geometry in the VSP data set presents a greater number of ray crossings per

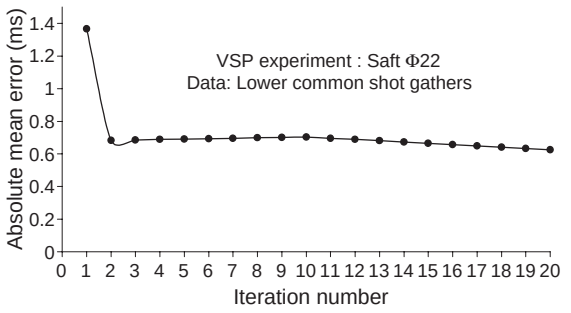

Fig. 11. Typical plot of mean absolute travel time for the VSP experiment F22.

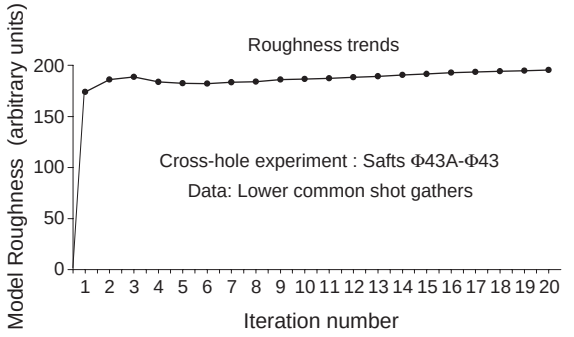

Fig. 13. Typical plot of complexity trends versus iteration number for the cross-hole experiments F43A and F43.

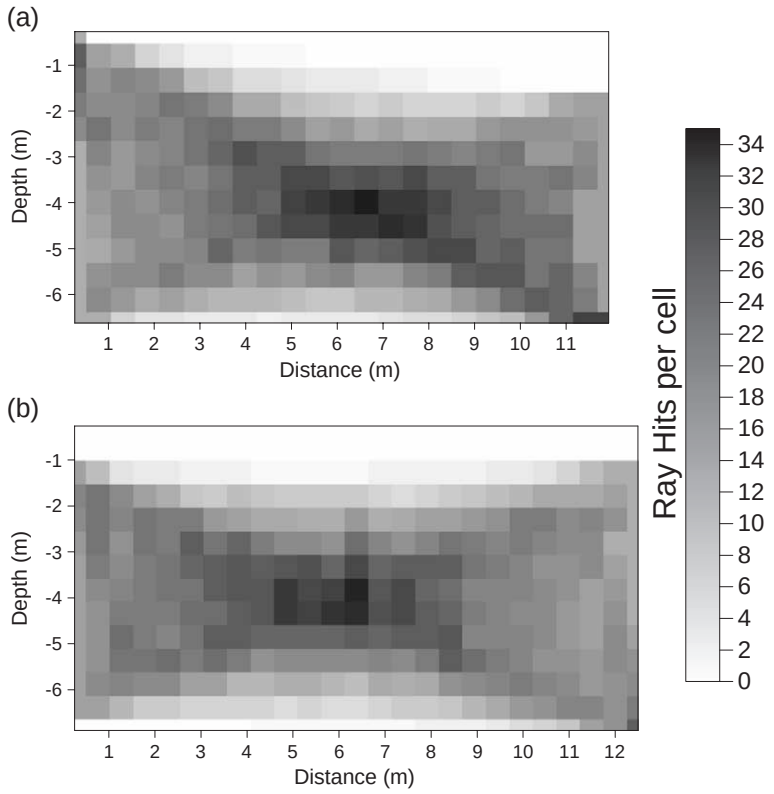

Fig. 14. Ray density maps for the cross-hole experiments F55–F54 (a) and F45A–F49 (b).

pixel, however, with limited angular coverage. The criteria of travel time misfit and stability between solution updates were used to understand and characterize the performance of the method. Results showed high-accuracy synthetic times, and consistent solution tomograms of least complexity verified by the geological mapping.

9. Results and interpretation

9.1. VSP experiment between shaft F22 and ground surface

The efficiency of the proposed seismic technique to resolve small size features in subsurface was checked by carrying out a calibration experiment at the site of shaft F22. A known natural cavity, unveiled during the excavation of shaft F22, was used to be the target to be detected with the seismic tomography technique. The image of the reconstructed velocity field shown in Fig. 17a can be divided into three main velocity zones: (1) the low-velocity (< 500 m/s) zone, A, at the top, attributed to the volcanic tephra layer, which was produced by the volcanic eruption and covered the entire island and the prehistoric settlement itself. The layer was removed during the systematic excavations by Professor Marinatos in 1967, and zone A is, today, a visible remainder of that layer; (2) zone B consisting of medium- to high-velocity (600–1000 m/s) structures, which is attributed to a layer of ruins of older age underlying the existing prehistoric settlement. That layer was verified during the shafts excavations; and (3) the lower zone, C, consisting of low- to high-velocity structures, which is attributed to the pyroclastic formation basement rock. The geologic record (Alexiadou and Fourniotis-Pavlatos, 2001) for shaft F22 reports a zone of compacted volcanic tuff with stones (Fig. 17b) between

1 and 2.2 m depth, a less compacted zone of the same material between 2.2 and 3.1 m depth, a tephra layer with a natural void of 1.2 m aperture between 3.1 and 4.3 m depth, and a zone of compacted tuff below 4.3 m depth. It should be mentioned here that the smearing of the high-velocity structures inside zones B and C along the main ray direction is probably due the limited angular ray coverage of the VSP layout.

In the zone of interest C, we can distinguish: (1) a high-velocity structure next to the top of the shaft, which is in very good correlation with the reported zone of tuff with stones (Fig. 17c); (2) a low-velocity (< 400 m/s) structure LV (Fig. 17a) located exactly in the same position with the reported natural cavity (Fig. 17b and c); and (3) a medium-velocity structure observed below LV, which is also in very good agreement with the reported zone of compacted tuff with stones.

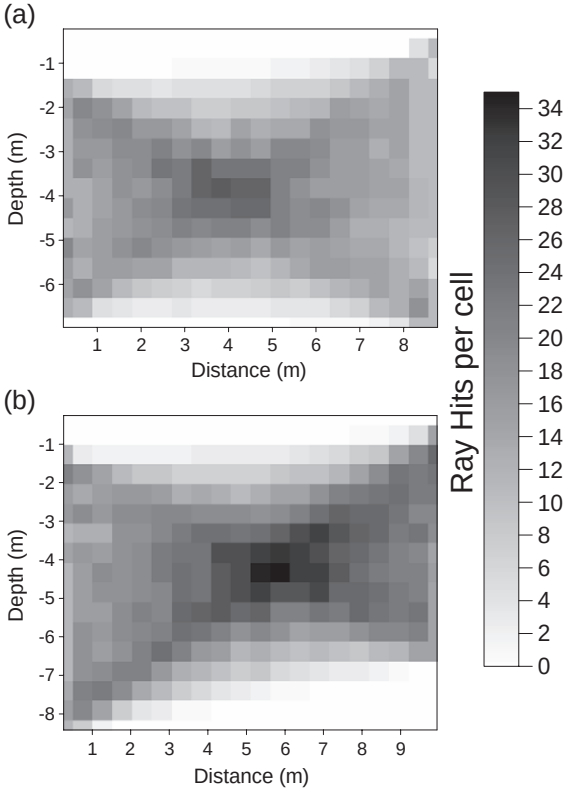

Fig. 15. Ray density maps for the cross-hole experiments F57–F56 (a) and F43A–F43 (b).

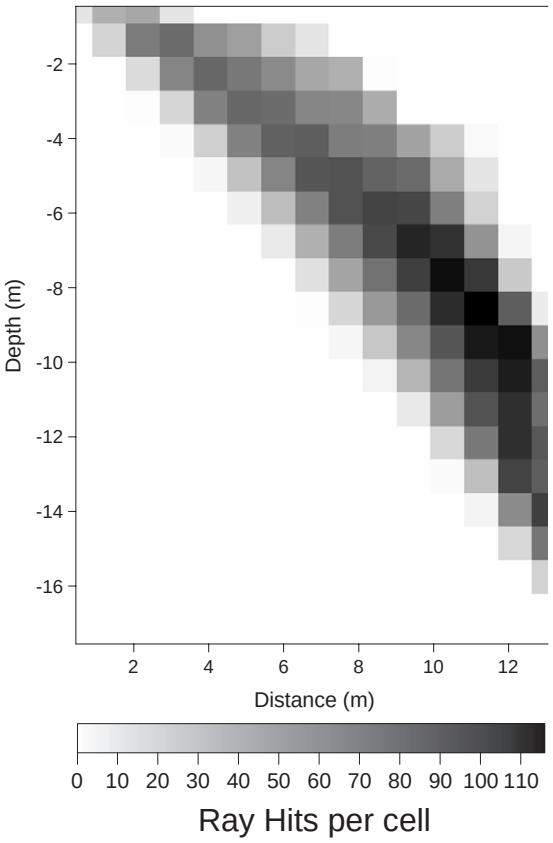

Fig. 16. Ray density map for the VSP experiment F22.

The calibration experiment indicated that the adopted seismic method is capable of resolving small size structures in depth.

9.2. Cross-hole experiments

9.2.1. Cross-hole experiment between shafts F56 and F57

The reconstructed velocity field of the imaged area (Fig. 18) is quite complex. Two low-velocity (LV1, LV2) and high-velocity (HV1, HV2) structures dominate a medium-velocity (500–800 m/s) environment. The geologic record (Alexiadou and Fourniotis-Pavlatos, 2001) for shaft F57 notes the dominance of tephra with volcanic stone intercalations. The zone between depths 1.1 and 3.4 m in shaft F57 is reported to consist of more compact materials with lower rippability.

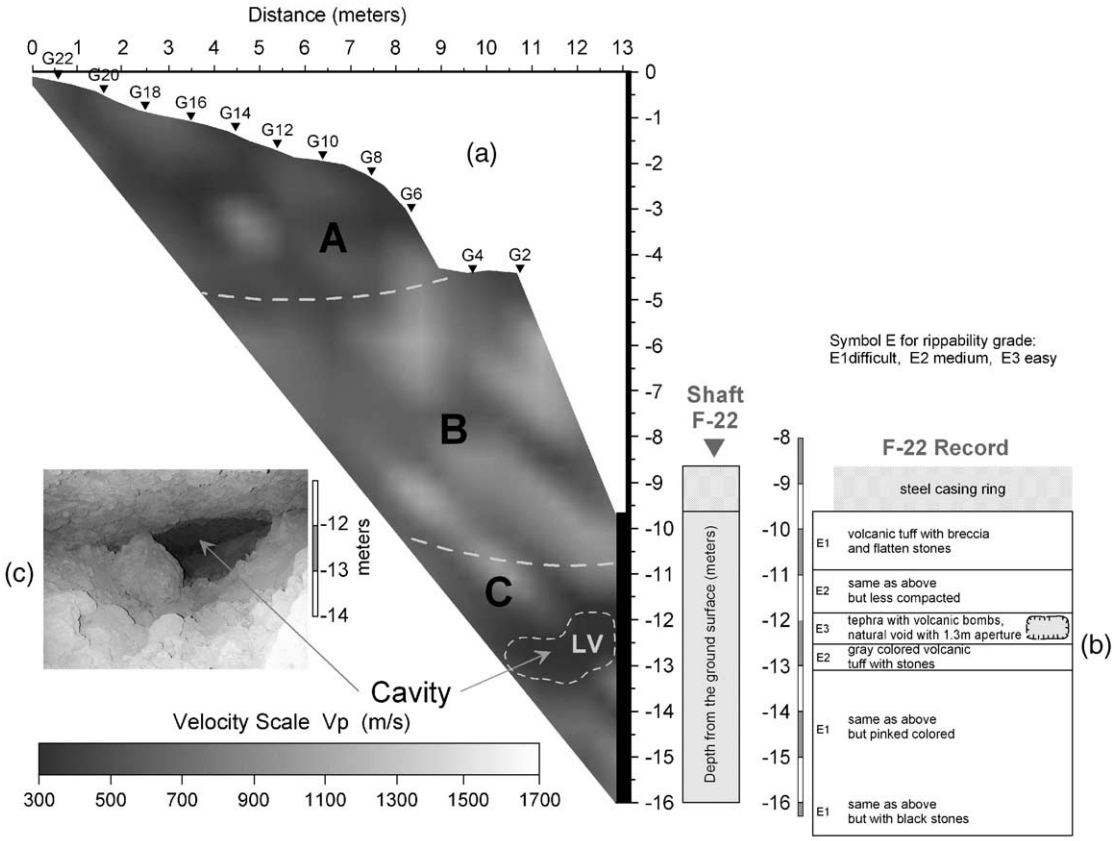

Fig. 17. Image of the reconstructed velocity field (a) with the geologic record for shaft F22 (b) and the cavity (c) unveiled during the shaft excavation (photo provided by Alexiadou and Fourniotis-Pavlatos, 2001).

It is definite that the high-velocity structure HV1 (Fig. 18) is very well correlated to this zone. According to the calibration test discussed in shaft F22, the low-velocity zones LV1 and LV2 are more likely to imply the existence of air-filled or semi-filled cavities situated close to the walls of the shafts.

9.2.2. Cross-hole experiment between shafts F55 and F54

The reconstructed velocity field is shown in Fig. 19. Low-velocity (<400 m/s) and high-velocity (>1000 m/s) structures dominate in a medium of velocities varying from 500 to 1000 m/s. The geologic record (Alexiadou and Fourniotis-Pavlatos, 2001) for shaft F55 reports a zone of medium to low rippability grades E2–E1, consisting of volcanic tuff with breccia and consolidated stones between 1.1 and 3.2 m depth; an underlying zone of higher rippability grade E3, consisting of loose volcanic tuff between 3.2 and 4.8 m depth, which is in a very good correlation with the low-velocity structure LV1 (Fig. 19); and a deeper zone of low rippability grade E1, consisting of very compact volcanic materials of sizable stones and volcanic bombs, being in very good agreement with the high-velocity zone HV2.

A zone of medium to low rippability grade E2–E1, between 2.7 and 5.5 m depth, consisting of volcanic tuff with breccia and volcanic bombs is also reported for shaft F54, which is in a very good correlation with

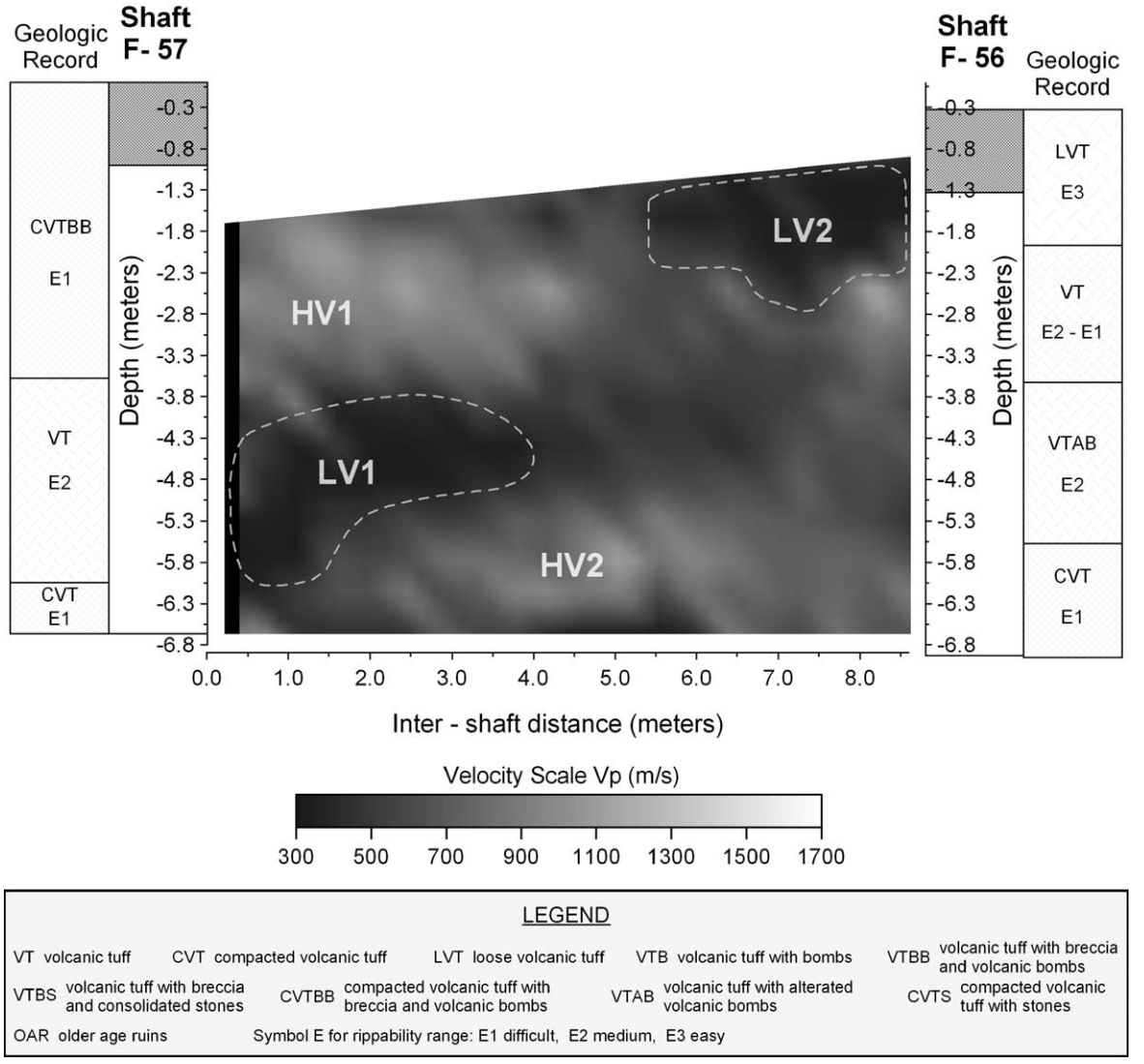

Fig. 18. Cross-hole velocity field between shafts F57 and F56.

the high-velocity zone HV3. Zones HV1 and HV3 seem to form a connected elongated zone observed in the upper part of the imaged area.

A cavity with aperture 1.1 m from the head of shaft F54, unveiled during the foundation works of the shaft, prevented the spread of geophones up to this depth with a consequent lack of imaging of area A (Fig. 19). The low-velocity zone LV2 implies the continuation of this cavity toward the imaged area.

9.2.3. Cross-hole experiment between shafts F49 and F45A

The image of the reconstructed velocity field (Fig. 20) is characterized by intermediate velocity values (1000 m/s). An impressive low-velocity structure, LV is observed next to the middle part of shaft F49. The geologic record (Alexiadou and Fourniotis-Pavlatos, 2001) for shaft F49 reports a low rippability zone of compacted volcanic tuff with stones up to 2.3 m depth, a medium rippability zone of volcanic tuff

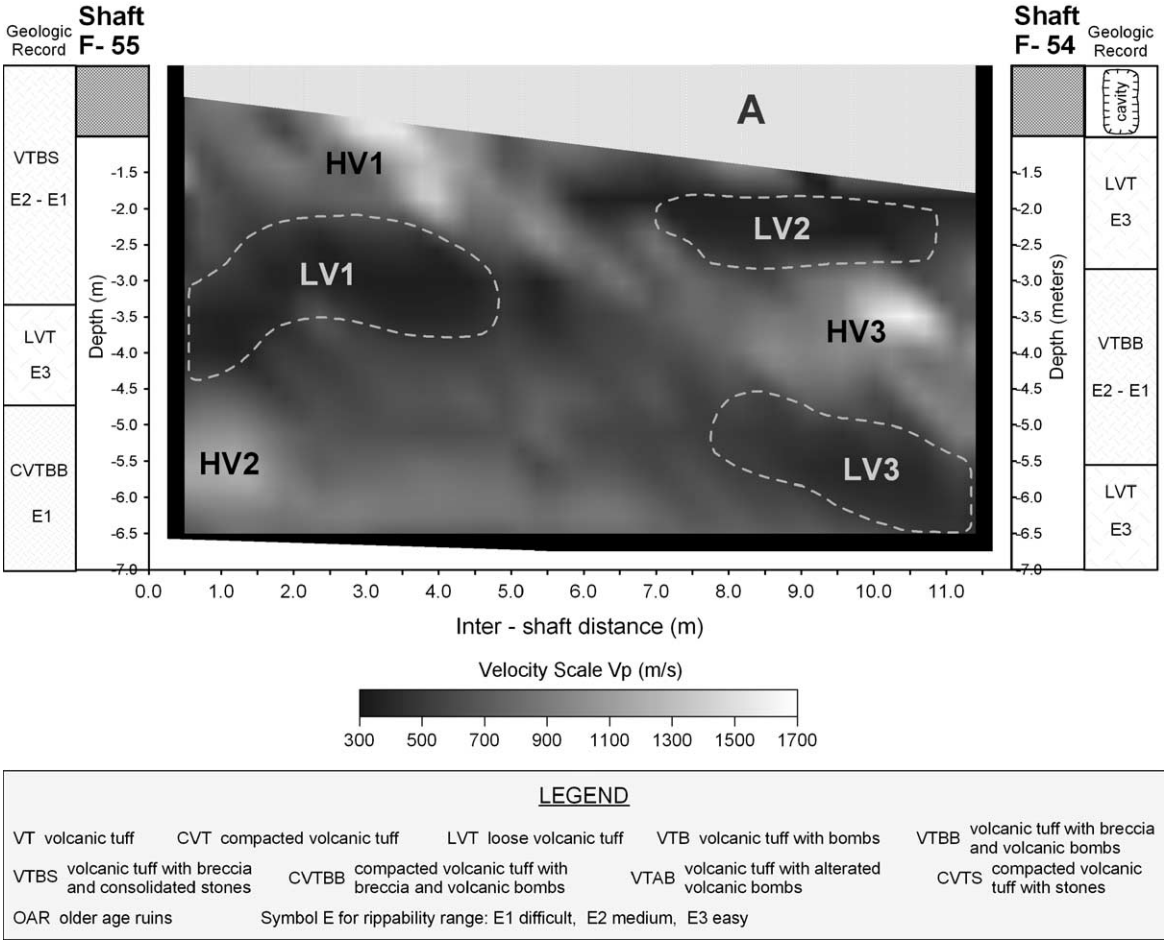

Fig. 19. Cross-hole velocity field between shafts F55 and F54.

with altered volcanic bombs between 2.3 and 2.7 m depth, a medium to high rippability zone E3–E2 of loose volcanic tuff between 2.7 and 4.6 m depth, and a zone of compacted volcanic tuff below 4.7 m depth.

The high-velocity structure observed next to the head of shaft F49 (Fig. 20) seems to be in a good correlation with the highly compacted zone of volcanic tuff with stones. However, since the ray-path coverage in this part of the imaged area is very poor, the high-velocity structure is considered rather as an artifact. The medium to high rippability zone between 2.7 and 4.6 m depth is consequently interpreted that, behind structure LV, a sizable cavity exists next to the wall of shaft F49.

9.2.4. Cross-hole experiment between shafts F43 and F43A

The image of the reconstructed velocity field (Fig. 21) is quite complex. Medium seismic velocities (600–1000 m/s), indicative of the pyroclastic formation basement, dominate the imaged area. Prominent low-velocity (LV1, LV2) and high-velocity (HV1, HV2, HV3) structures are observed in the imaged area. The geologic record (Alexiadou and Fourniotis-Pavlatos, 2001) for shaft F43A reports a cavity between depths 1 and 3.5 m, unveiled during the shaft excavation. A zone of ruins of older age is also reported between depths 3.5 and 4.5 m, which give a very good explanation for the lower part of the high-velocity structure HV1 (Fig. 21) imaged

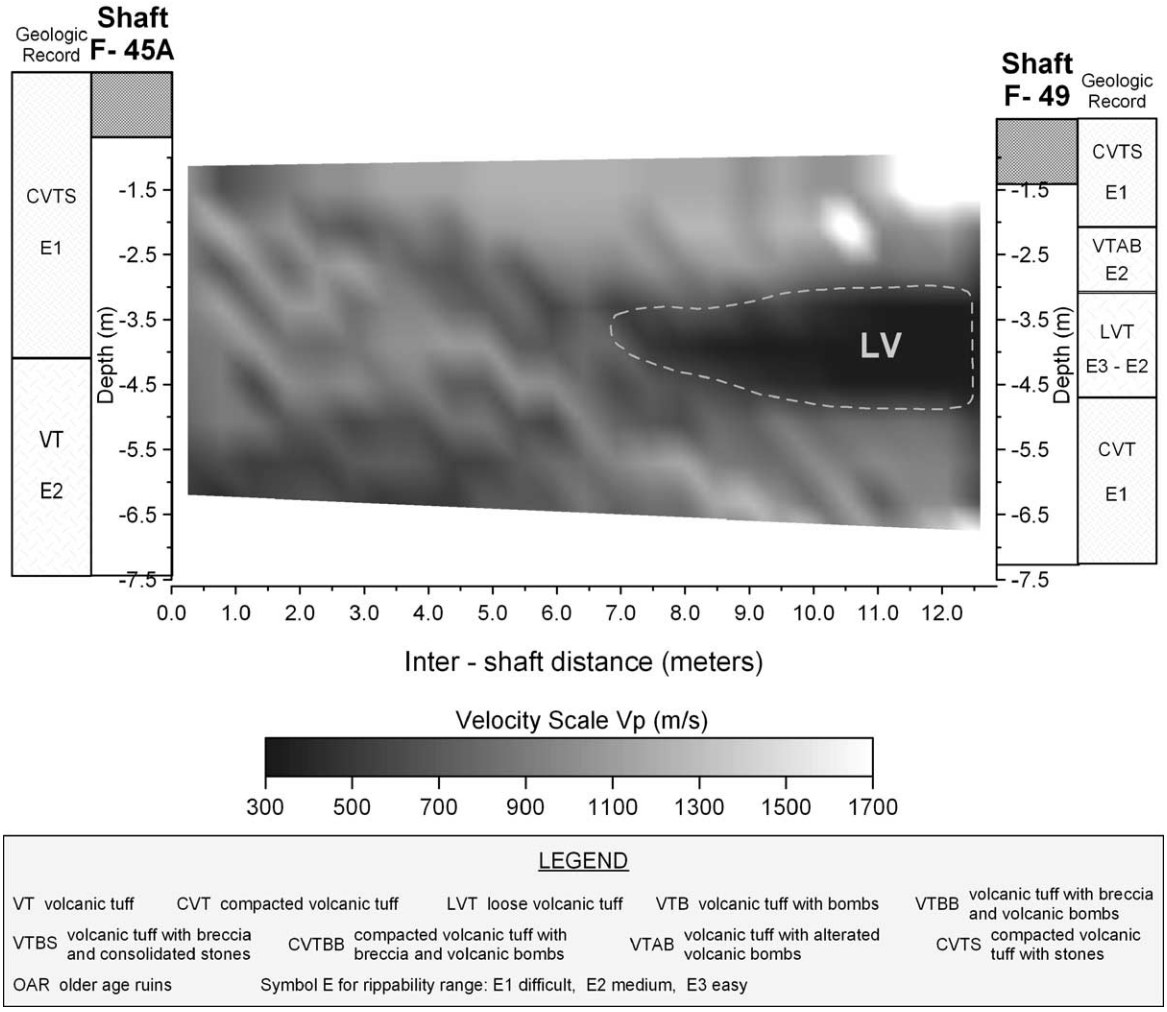

Fig. 20. Cross-hole velocity field between shafts F45A and F49.

exactly in the same position. The upper part of structure HV1 is easily explained by the existence of a screen barrier of older-age ruins reported to build the back wall of the cavity. The low-velocity structure LV2 resembles structure LV1 both in shape and seismic velocity. We believe that LV2 is attributed to a hidden cavity situated close to the wall of the shaft. The geologic report (Alexiadou and Fourniotis-Pavlatos, 2001) for shaft F43A reports a low rippability zone of compacted volcanic tuff with breccia and volcanic bombs between 6.3 and 8.5 m depth. This zone explains very well the high-velocity feature HV3 observed at the same position.

10. Discussion and conclusions

An accurate high-resolution seismic inversion technique was used to explore the pyroclastic formation basement at the Akrotiri archaeological site of Thera Island. The survey was carried out in the context of a large-scale project in which the old protective roof cover of the monuments is being replaced by a new, elaborate, environmentally friendly structure, which will be supported by 95 pillars embedded in an equal number of foundation shafts drilled into the formation basement. The target of the geophysical investigation was the detection of man-made or natural cavities, the presence

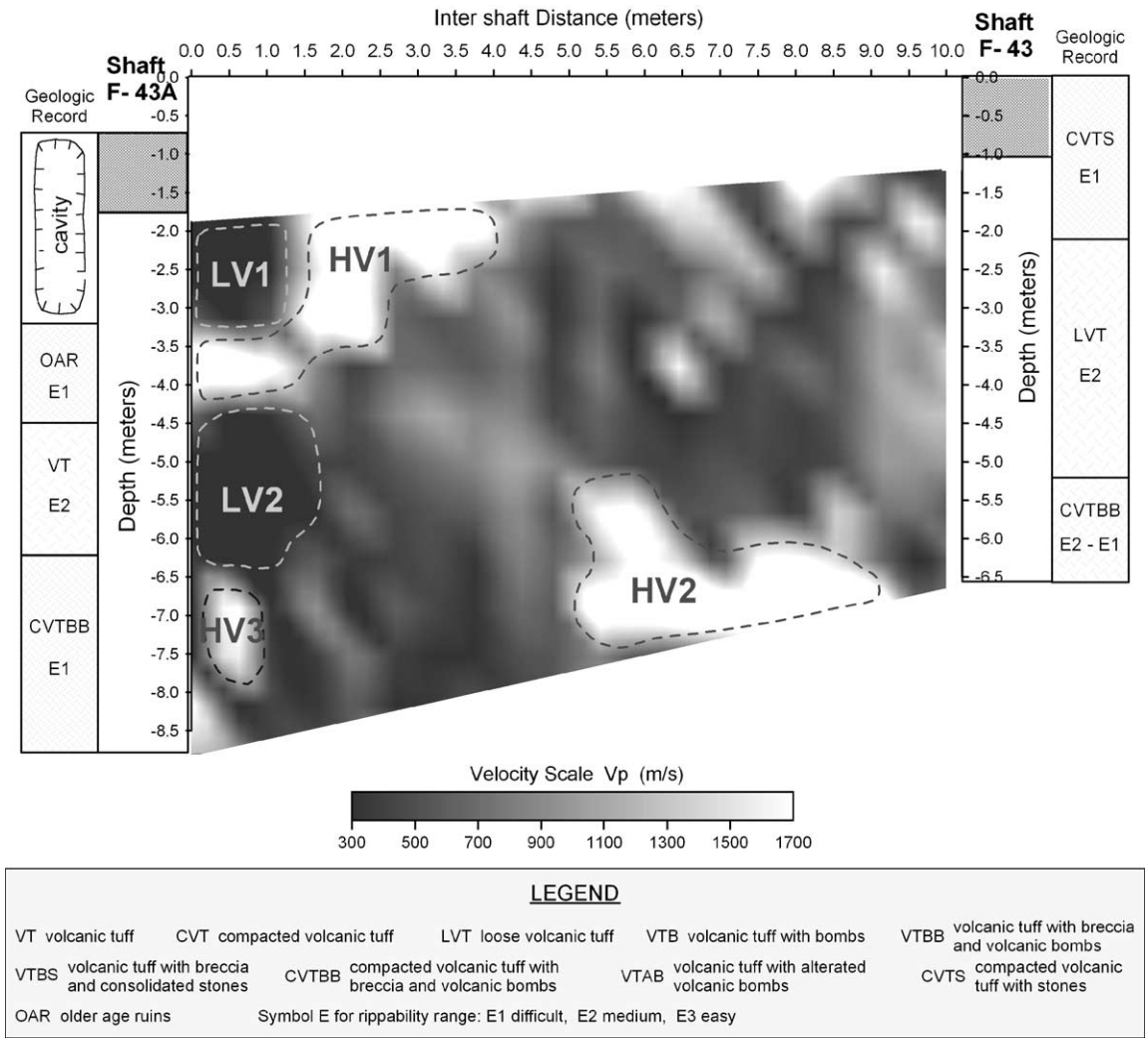

Fig. 21. Cross-hole velocity field between shafts F43A and F43.

of which was discovered during the excavation of the shafts.

Seismic cross-hole and VSP experiments were performed to detect the voids because their presence might affect the structure stability of the structure during an earthquake. A number of synthetic examples and a calibration experiment at a shaft with a known natural cavity clearly indicated that the tomographic inversion is capable of providing highly resolved 2-D velocity models from an adequate number of travel time data. Within the resolution limits of the method, all of these tests produced good results. Acquisition geometry measurements were very accurate and high-quality seismic records were obtained.

The seismic tomogram for the VSP experiment that served as a calibration test revealed the existence of three layers of interest: the top zone A, which is the remainder of the tephra layer that was removed during the systematic excavations; the middle zone B of ruins of older age verified during the excavations of the foundation shafts; and the lower zone C attributed to the pyroclastic formation basement.

The corresponding cross-hole tomographic sections reveal the same layer sequence, with seismic velocities varying from 600 to 1000 m/s, and are of

interest from an archaeological point of view. The reconstructed velocity fields were quite consistent with the expected velocities and the structures of interest based on geologic logs recorded during the excavation of the shafts.

A set of stability tests was run to check the consistency of the inversion method. The sequence of checks began with a visual evaluation of the velocity anomalies and the amplitude of oscillation between models from successive iterations. Using such inspections as a convergence check is highly subjective and, for that reason, a set of statistical measures was used to determine the reliability of the models.

Travel time residuals verified the validity of the final velocity depth sections, while model complexity trends showed a consistency between models after a certain number of iterations. This consistency indicated that the relative high and low variations in velocity were, in most of the cases, genuinely representative of the arrival time data sets and not some artifacts of the numerical scheme.

Acknowledgments

We would like to express our thanks to Professor Christos Doumas, Director of the Archaeological Excavations at Akrotiri, Thera Island, for permission to publish the results leading to this article. Special thanks are also extended to Dr. Nikos Fintikakis, architect of the project at Akrotiri. for his exceptional collaboration and technical support. John Washbourne and an anonymous reviewer provided constructive criticisms that improved significantly the quality of the paper. We also thank Dr. Nick Bernitsas, Senior VP and Chief Technology Officer, GXT Technology, for his helpful comments and suggestions. This work is part of a PhD research program funded by IRAKLEITOS, Fellowships for Research, ENVIRONMENT, of the National and Kapodistrian University of Athens.

References

Alexiadou, M.C., Fourniotis-Pavlatos, C., 2001. Geological supervision of shafts excavations at Akrotiri on Thera Island. Technical Report, Archaeological Society at Athens, Athens.

Bohm, G., Vesnaver, A., 1999. In quest of the grid. Geophysics 64, 1116–1125.

Bois, P., La Porte, M., Lavergne, M., Thomas, G., 1971. Essai de determination automatique des vitesses sismiques par mesures entre puits. Geophys. Prospect. 19, 42–83.

Bregman, N.D., Bailey, R.C., Chapman, C.H., 1989. Crosshole seismic tomography. Geophysics 54, 200–215.

Bube, K.P., and Langan, R.T., 1995. Resolution of the crosswell tomography with transmission and reflective traveltimes. Stanford Tomography Project Vol. 6, 1995 Annual Report.

Dines, K.A., Lytle, R.J., 1979. Computerized geophysical tomography. Proc. IEEE 67, 471–480.

Hatton, L., Worthington, M.H., Makin, J., 1986. Seismic Data Processing: Theory and Practice. Blackwell Scientific Publications, pp. 156–162.

J&P (Hellas) SA, IMPREGILO SpA, AVAX SA, GNOMON SA, Constructing Group of Engineers, 2001. Ground plan maps of the excavated shafts area at Akrotiri on Thera, Athens.

Khalil, A.A., Stewart, R.R., Henley, D.C., 1993. Full-waveform processing and interpretation of kilohertz crosswell seismic data. Geophysics 58, 1248–1256.

Koloski, J.W., Schwarz, S.D., Tubbs, D.W., 1989. Geotechnical properties of geologic materials: engineering geology in Washington, volume 1. Bull.-Wash., Div. Geol. Earth Resour. 78.

Lazaratos, S.K., Rector, J.W., Harris, J.M., Van Schaack, M., 1993. High-resolution, crosswell, reflection imaging: potential and technical difficulties. Geophysics 58, 1270–1280.

Leveque, J., Rivera, L., Wittlinger, G., 1993. On the use of the checker-board test to asses the resolution of tomographic inversions. Geophys. J. Int. 115, 313–318.

Louis, F.I., 2001. Cross-hole seismic tomography in prospecting for cavities at the archaeological excavation area on Thera Island Greece. MSc Thesis, University of Leeds, UK.

Louis, I.F., Makropoulos, C.C., 2001. Geophysical investigations at Akrotiri archaeological site on Thera Island. Technical Report, Archaeological Society at Athens, Athens.

Mason, I.M., 1981. Algebraic reconstruction of a 2-D velocity inhomogeneity in the High Hazles seam of Thoresby Colliery. Geophysics 46, 298–308.

McMechan, G.A., 1983. Seismic tomography in boreholes. Geophys. J. R. Astron. Soc. 74, 601–605.

Peterson, J.E., Paulsson, B.N.P., McEvilly, V., 1985. Applications of algebraic reconstruction techniques to cross-hole seismic data. Geophysics 50, 1566–1580.

Philips, W.S., Fehler, M.C., 1991. Travel time tomography: a comparison of popular methods. Geophysics 56, 1642–1643.

Pratt, R.G., Chapman, C.H., 1992. Traveltime tomography in anisotropic media II: application. Geophys. J. Int. 109, 20–37.

Pratt, R.G., Goulty, N.R., 1991. Combining wave equation imaging with traveltime tomography to form high resolution images from crosshole data. Geophysics 56, 208–224.

Pratt, R.G., McGaughey, W.J., Chapman, C.H., 1993. Anisotropic velocity tomography: a case study in a near surface rockmass. Geophysics 58, 1748–1763.

Rector, J., Washbourne, J., Alonso, A., Cherrington, M., Delonas, T., Hugging, R., 1996. 3-D seismic exploration for the Victorio

Peak treasure. 66th Ann. Internat. Mtg.: Soc. Expl. Geophys. Expanded Abstracts, pp. 2076–2080.
Schaack, M., 1995. Crosswell traveltime tomography using direct and reflected arrivals. Part 2: examples. Stanford Tomography Project Vol. 6, 1995 Annual Report.
Smith, K., 1984. Seismic Tomography in boreholes using an algebraic reconstruction technique. MSc Thesis, Colorado School of Mines, pp. 2–25.
Vesnaver, A., Böhm, G., Madrussani, G., Petersen, S., Rossi, G., 1999. Tomographic imaging by reflected and refracted arrivals at the North-Sea. Geophysics 64 (6), 1852–1862.
Washbourne, J., Rector, J., Alonso, A., 1998. Treasure hunting with direct arrival transmission imaging. Lead. Edge 17 (07), 927–933.